Deploying Fixed Wing Unoccupied Aerial Systems (UAS) for Coastal Morphology Assessment and Management

Authors: Seymour, A.C., Ridge, J.T., Rodriguez, A.B., Newton, E., Dale, J., et al.

Source: Journal of Coastal Research, 34(3) : 704-717

Published By: Coastal Education and Research Foundation

URL: https://doi.org/10.2112/JCOASTRES-D-17-00088.1

Journal of Coastal Research	34	3	704–717	Coconut Creek, Florida	May 2018

TECHNICAL COMMUNICATIONS

www.cerf-jcr.org

Deploying Fixed Wing Unoccupied Aerial Systems (UAS) for Coastal Morphology Assessment and Management

A.C. Seymour†*, J.T. Ridge†‡, A.B. Rodriguez‡, E. Newton†, J. Dale†, and D.W. Johnston†

†Division of Marine Science and Conservation
Nicholas School of the Environment
Duke University Marine Laboratory
Beaufort, NC 28516, U.S.A.

‡Institute of Marine Sciences
University of North Carolina at Chapel Hill
Morehead City, NC 28557, U.S.A.

ABSTRACT

www.JCRonline.org

Seymour, A.C.; Ridge, J.T.; Rodriguez, A.B.; Newton, E.; Dale, J., and Johnston, D.W., 2018. Deploying fixed wing unoccupied aerial systems (UAS) for coastal morphology assessment and management. *Journal of Coastal Research,* 34(3), 704–717. Coconut Creek (Florida), ISSN 0749-0208.

Accurate measurement of the morphology and distribution of coastal habitats is critical for understanding the function of coastal environments, assessing the resilience of coastal communities, and managing the coastal zone effectively. Unoccupied aerial systems (UASs, also known as unmanned aerial vehicles) and structure from motion (SfM) photogrammetry may be optimal for coastal surveys around small- or medium-sized municipalities, but guidance is needed to identify appropriate equipment configurations. Digital surface models (DSMs) from UAS equipped with mapping and survey-grade GPS units were processed with and without ground control point (GCP) correction, and their accuracy was compared to terrestrial laser scanner (TLS) derived DSMs and global navigation satellite system (GNSS) checkpoints. Four UAS sorties were flown over an active fetch-limited barrier island in North Carolina, which was concurrently surveyed with TLS and GNSS. Average DSM vertical accuracy from real-time kinematic (RTK)-equipped UAS improved from 0.081 m error to 0.032 m error after GCP correction, and the average elevation range between surfaces improved from ~0.17 m to ~0.05 m. In areas with low dunes, the UAS DSM was an average of 0.042 m away from the TLS DSM and was closer to the GNSS survey checkpoints. In vegetated areas, this distance increased to 0.082 m because of TLS occlusion effects. The SfM process-generated elevation artifacts in areas of imagery with homogenous texture, such as the foreshore and sun angle, likely plays an important role when surveying sandy beach environments. The RTK-equipped UAS and UAS data processed with GCPs yield DMSs with similar accuracy to those derived from TLS but are a superior choice for municipal-scale surveys because of lower operating costs, greater areal coverage, and lower environmental impact.

ADDITIONAL INDEX WORDS: *Vulnerability assessment, coastal resilience, terrestrial laser scanning, structure from motion, coastal erosion, coastal management*.

INTRODUCTION

Accurate measurement of the morphology, distribution, and species composition of coastal habitats is critical for understanding the effects of physical processes, climate change, and anthropogenic modifications on the function of coastal environments as well as human infrastructure. Metrics such as beach and dune elevation, width, and vegetation cover can be used to predict coastal resilience in the face of hurricanes, tsunamis, and sea-level rise. When combined within a GIS, these coastal surveys can be applied to vulnerability assessments by estimating coastal inundation and storm surge that threatens infrastructure or that impacts habitat during extreme weather events (Casella *et al*., 2014; Hart and Knight, 2009; Klemas, 2009).

Surveys of beach and dune structure usually involve some amount of *in situ* human effort. While satellites can be used to map locations of coastal infrastructure, vegetation, and long-term barrier island migration, methods such as LIDAR and terrestrial laser scanning (TLS) are needed to record accurate elevation maps of beach and dune systems. The TLS surveys can have excellent spatial resolution, but they are time consuming, especially around complex terrain such as vegetation or dunes. These complex features often cause missed laser returns and occlusion effects (Eltner and Baumgart, 2015; Eltner, Mulsow, and Maas, 2013; Feagin *et al*., 2014), requiring multiple scanner deployments. This factor typically limits the scale of TLS surveys to 0.05 km^2 or less (Barneveld, Seeger, and Maalen-Johansen, 2013; Feagin *et al*., 2014; Schneider *et al*., 2012; Schürch *et al*., 2011) and prevents the method from being used to assess coastal resilience at municipal scales, such as beaches or dune systems 2–5 km in length. Conversely, aerial-based LIDAR is an efficient means of surveying areas at a regional scale with a resolution adequate for informing management and can effectively parse vegetation elevation

---

DOI: 10.2112/JCOASTRES-D-17-00088.1 received 21 May 2017; accepted in revision 11 September 2017; corrected proofs received 3 November 2017; published pre-print online 14 December 2017.

*Corresponding author: alexander.c.seymour@duke.edu

from ground elevation. However, aerial LIDAR is traditionally deployed on manned aircraft, which inherently involves risk for flight personnel (Sasse, 2003). Manned flights can also be prohibitively expensive at smaller scales (Klemas, 2015) and cannot typically be deployed on short notice or with high frequency (Casella *et al.*, 2014), making it difficult to schedule surveys before and after storms or around smaller municipalities.

Over the last decade, researchers have combined unoccupied aerial systems (UASs)-based image collection with a data processing workflow called structure from motion (SfM), outputting three-dimensional (3D) digital surface models (DSMs) of various terrain and habitat types. Small-scale studies have applied this approach to coastal beach and dune systems (Casella *et al.*, 2014; Delacourt *et al.*, 2009; Gonçalves and Henriques, 2015; Harwin and Lucieer, 2012; Papakonstantinou, Topouzelis, and Pavlogeorgatos, 2016), demonstrating that UAS-derived DSMs can achieve a similar resolution and accuracy as TLS (Mancini *et al.*, 2013). While most UASs used in these studies were relatively low-endurance rotary-wing craft flying at low altitude, small fixed-wing UASs now exist with an aerial endurance of an hour or more and the potential to collect large datasets (0.5–1 km^2) in a single flight (*e.g.*, senseFly eBee plus, Altavian Nova). UAS can be a powerful survey tool for informing coastal management around small- and medium-sized municipalities; their simplified logistics and relatively low cost of operation can often allow for flexible deployment, and they can be used to collect datasets just ahead of and after storm systems.

The SfM workflow creates image mosaics by applying the scale invariant feature transformation (SIFT) algorithm to collections of overlapping photos collected by the UAS, identifying pixels called "keypoints" that represent the same feature in multiple images. SIFT achieves this by scanning color or reflectance gradients, which, unlike raw pixel values, remain consistent around objects of interest in multiple images, even under a range of image scales, rotations, or exposure conditions. Once calculated, keypoints are used to triangulate the position and orientation of each camera. An additional step, called "densification," combines the above position information with image content and the sensor's geometry, filling in the area between keypoints with a dense point cloud that can be interpolated. The 3D surfaces can be produced with relative accuracy in the absence of GPS input, but for surfaces to be spatially scaled to global or local datums, images must include ground control points (GCPs), be geotagged by a system onboard the UAS, or both.

Many UAS include onboard global navigation satellite system (GNSS) modules that can be used to execute autonomous flights and geotag images. These systems vary in precision, and accuracy testing of these modules is generally conducted by the manufacturer and provided within the product specification. Most mapping-grade GNSS modules include 2–5 m of horizontal and vertical error (Wing, Eklund, and Kellogg, 2005). Some units make use of additional features to improve accuracy, such as access to multiple satellite constellations, or can read additional carrier frequencies to correct for ionospheric disturbance (Karsky, 2004). Differential GPS units are more precise and connect to a reference station that is constantly providing error corrections to the GNSS module (Karsky, 2004), potentially reducing error to decimeter levels. Survey-grade real-time-kinematic (RTK) GPS units are high precision that connect to reference stations and also utilize the phase (wavelength) of each satellite signal to better calculate position, further reducing error down to subcentimeter levels (LaMarca and Lara, 2008). For UAS mapping purposes, this high precision capability allows users to forgo GCP deployment in some situations, though the accuracy of an outputted DSM is the product of the environment being imaged, the number of discernable keypoints, and the flight plan used, as well as the accuracy of the installed GPS unit. While the advantages of mapping-grade GNSS, survey-grade RTK GNSS, and GCP deployment are known, the impact of the beach and dune environments on these advantages has yet to be fully assessed.

The SfM approach often generates elevation artifacts when constructing a DSM over sections of terrain with low image texture where few keypoints are discernable. This problem has been reported in multiple SfM-based software packages (Bühler *et al.*, 2017; Gross and Heumann, 2016; Mancini *et al.*, 2013) and is inherent to the SfM approach. In a coastal environment, artifacts may occur around low-contrast patches of homogenous-colored sand or mud or when light-colored sand is overexposed. Artifacts can inject uncertainty into change analysis (Schneider *et al.,* 2012) or distract from visual DSM presentation, and while photogrammetry software allows for elevation surface or point cloud editing, modifying larger municipal-scale datasets can be time consuming. Discussion of the specific environmental conditions leading to these artifacts has already begun for glaciers (Gómez-Gutiérrez *et al.*, 2015) and for snow-covered mountains (Bühler *et al.*, 2017), but additional guidance regarding how to predict, avoid, or eliminate artifacts in a coastal context is needed.

This paper evaluates the effectiveness of small, fixed-wing UASs equipped with and without onboard RTK GPS systems in the collection and presentation of elevation datasets that can be used effectively in coastal management. Specifically, the accuracy of UAS-derived DSMs of beaches and dunes in eastern North Carolina is compared to TLS-derived DSMs and GNSS point surveys. In addition, the different artifacts that these methods generate are compared, and accuracy results as well as artifact coverage are parsed by habitat type. The paper concludes with guidelines regarding equipment selection and flight planning in the context of monitoring missions scaled to a small municipality.

METHODS

Aerial, GNSS, and TLS surveys were conducted on 2 June 2016 at Bird Shoal and Bulkhead Shoal (approximately 34.709817, –076.673572, decimal degrees, WGS 1984), part of an active fetch-limited barrier island (Pilkey, Cooper, and Lewis, 2009) and salt marsh complex immediately seaward of the town of Beaufort, North Carolina, and the Duke University Marine Lab (Figure 1). The study area includes sparse

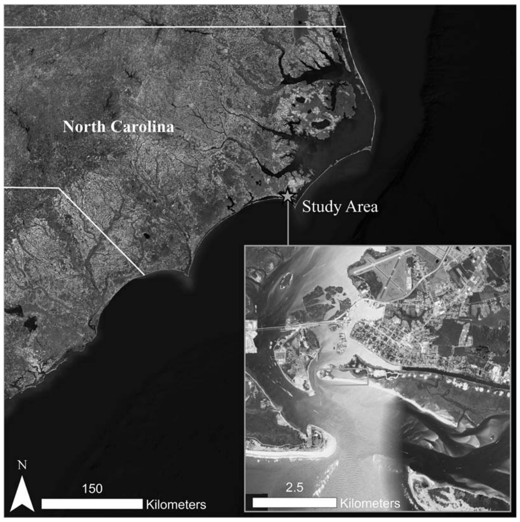

Figure 1. The location of our study area, south of Beaufort, North Carolina.

maritime forest, salt marsh, oyster beds, sandy beach, and a low-lying vegetated dune system.

GNSS Surveys and GCPs

Prior to UAS and TLS data collection, the x, y, and z coordinates of 60 GNSS points were recorded with a Trimble R8s survey-grade GPS system, with average horizontal and vertical errors of 0.011 m and 0.021 m, respectively. Ten of these points were represented by large 1.21-m^2 square mats with an iron cross pattern designed for aerial recognition. Because of a shortage of large targets, an additional three points were represented by 0.09 m^2 black square mats with centered 8-cm-diameter circular reflectors. Six of the large targets were designated as GCPs for rectifying aerial imagery. The remaining seven targets (four large targets and three small targets) were reserved as horizontal and vertical checkpoints to help assess accuracy because horizontal assessment requires a visual representation. The remaining 47 points acted strictly as vertical checkpoints, which do not require visual representation in imagery. An additional 16 elevated cylindrical reflectors (10-cm diameter) designed for registering TLS data were deployed and geolocated.

Small Unoccupied Aerial Systems and TLS

Three aerial surveys were performed with the senseFly eBee RTK, a small, fixed-wing UAS with a wingspan of 96 cm, a weight of 0.73 kg, and powered by a rear-mounted electric motor. The aircraft is equipped with a survey-grade RTK GPS system (specifications are found in Appendix A) with a marketed horizontal and vertical accuracy down to 3 cm and 5 cm, respectively (senseFly, LLC). An additional aerial survey was conducted with a standard senseFly eBee—an airframe with a mapping-grade GPS system with a marketed horizontal and vertical accuracy of 2.5 m and 3 m, respectively (specifications found in Appendix A), but otherwise identical to the craft previously described. The RTK GPS system has superior accuracy because of several features, but the most meaningful are the ability to connect to the L2 satellite frequency, as well as actively communicate with a reference station less than 1 mile away (CORS ID: NCBE).

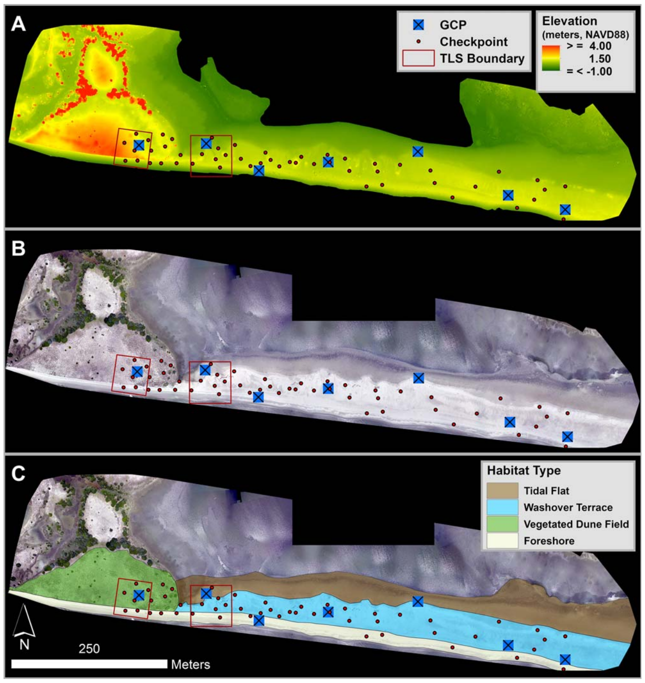

Figure 2. (A) DSM and (B) orthomosaic processed from the combined imagery of Flights 1–3, with locations for GCPs, checkpoints, and TLS plot boundaries. (C) Basic habitat coverage of the study area showing the foreshore, washover terrace, tidal flat, and vegetated dune field. Though only six GCPs were used for georectification, seven are shown on the map because Flight 1 had a slightly smaller eastern extent than the other flights and made use of an alternate GCP, which functioned as a checkpoint for other flights. (Color for this figure is available in the online version of this article.)

The three eBee RTK surveys and single-standard eBee survey were conducted consecutively on 2 June 2016, with each flight covering approximately 0.2 km^2. The flights imaged roughly the same spatial footprint over Bird and Bulkhead Shoal, though the flight lines and photo points were arrayed slightly differently. All flights were automated, with flight track lines and shutter trigger points preprogrammed in the eMotion2 ground control software program (senseFly, Switzerland) and uploaded to the UAS prior to launch. All imagery was collected off-nadir at a 7° pitch angle, and the planned UAS mission altitude was 70 m above sea level, corresponding to a $\sim$2 cm ground sampling distance (GSD).

Imagery was collected by a fixed-position, belly-mounted 18.2 megapixel RGB (red, green, blue) camera (Sony DSC-WX220) loaded into the UAS's payload bay, collecting at a 4896×3672 pixel image format. The camera used automatic shutter speed selection, and images were planned with 80% longitudinal and 75% lateral overlap between neighboring photos.

Concurrently, two 2500 m^2 plots were scanned with a RIEGL 3D LMSZ210ii TLS; plot boundaries are shown in Figure 2. Each plot contained different habitats. The vegetated-dune plot encompassed a forebeach, a backbeach, and a scarp separating

Table 1. *Flight and dataset statistics for sorties. Flights 1–3 were conducted with a UAS equipped with a survey-grade RTK GPS and Flight 4 with a UAS equipped with a mapping-grade GPS. Note the loss of RTK fix during Flight 3 halfway through the sortie. This means that the GPS unit continued to geotag photos but did so with an accuracy closer to that of a mapping-grade GPS.*

Flight #	Start Time (GMT)	Duration (min)	Area Covered (km^2)	Average Point Cloud Density (pts/m^3)	Max Wind Speed (m/s)	Intended GSD (cm^2/px)	Actual GSD (cm^2/px)	Solar Azimuth (angle, °)	Solar Elevation (angle, °)	Notes
1	1652	19	0.169	200	9.0	2.5	2.54	167.02	77.31	Mission ended prematurely
2	1722	14	0.176	309	7.8	2.0	2.11	198.57	77.00	
3	1749	18	0.179	331	8.3	2.0	2.12	221.25	74.20	RTK fix lost after 1758
4	1818	17	0.184	305	7.3	2.0	2.14	237.32	69.66	-

a vegetated dune field from the backbeach (~2.5 m elevation change). The washover plot included a forebeach, sparsely vegetated low-lying dunes, and a washover terrace. Each plot was imaged from four different scan positions to illuminate the 3D structure and mitigate occlusion effects. The four scan positions were referenced using the same eight cylindrical reflector targets distributed around each plot on elevated (1.335 m or 2.585 m above the ground) level survey rods.

Mosaic and DSM Processing

Imagery from each flight was processed separately in the software program Pix4D Mapper to generate four individual point clouds (three for the RTK eBee and one for the standard eBee). The same processing settings were used to generate all point clouds; the keypoint image scale was set to Full to improve keypoint generation on areas of the imagery with homogenous texture, and the default standard camera calibration method was used. Pix4D outputted a DSM for each flight using an inverse distance weighting method, with default noise filtering and surface smoothing options permitted for this step. These filtering settings generally exclude small groups of points from DSM interpolation that are isolated from points composing contiguous surfaces and automatically smooth sharp sections of the point cloud, which is a standard setting for processing images of non-urban areas. Six iron-cross patterned GCPs were used for georectification, outputting the DSMs in the WGS1984 UTM Zone 18N horizontal projection and the North American Vertical Datum of 1988 (NAVD88) vertical datum. Additionally, the RTK flights were processed without GCP correction to assess the native accuracy of the airborne RTK system.

For an additional product, the same workflow was used to process images from all three eBee RTK flights together, resulting in a single DSM. This was done to help assess processing methods that can affect DSM accuracy and artifact generation. Processing all imagery in a single project increased photo overlap and the density of the point cloud, increasing the number of keypoints that could be matched.

The TLS point clouds were generated using RiSCAN Pro software (RIEGL LMS, 2013), and nonground points associated with vegetation, elevated reflectors, people, *etc*., were classified and removed using the MARS 7 software package (Merrick, 2017). A 5-cm raster DSM was then generated through a universal kriging approach using the Surfer 11 software package (Golden Software, 2012). Additionally, the point cloud from the single-most accurate GCP-corrected RTK flight (Flight 2) was processed to a 5-cm cell resolution in Surfer 11 so that TLS and UAS-derived DSMs could be directly compared without bias from the different interpolation method used by Pix4D. Flight 2 was chosen because its GCP-corrected DSM was closest to the GNSS checkpoint elevations, which were the accuracy benchmark for this study.

Accuracy Analysis

Most of the GNSS points were used as checkpoints to assess the accuracy of outputs. The x, y locations of seven of these points were registered in Pix4D, allowing the program to automatically calculate horizontal root mean square (RMS) error. To assess the vertical accuracy of the DSMs, 53 points from the GNSS survey were imported into a GIS (Esri ArcMap, version 10.4.1) as point shapefiles, excluding the six points used to georectify the DSMs. The sample tool was used to append the underlying elevation value on a given DSM to each GNSS point. This allowed for calculation of the vertical RMS error for each DSM using the GNSS surveys as a reference.

TLS and UAS DSM Comparison

The TLS and UAS DSMs generated from universal kriging were compared by subtracting the UAS NAVD88 elevation from the TLS elevation, resulting in a pixel by pixel elevation difference between the two surfaces.

The elevations of the TLS and UAS-derived DSMs were also subtracted from the GNSS points within the TLS boundaries, converting the results to absolute values. For this step, additional GNSS points were included than were described in the larger accuracy analysis (six additional points at the vegetated dune plot, and one additional point at the washover terrace plot). The results represented the non-negative vertical distance of each DSM from the GNSS points. Because the samples were not normally distributed, a Wilcoxon Rank Sum test was used to determine whether the TLS or UAS surface was closer to the GNSS checkpoints.

RESULTS

The most extensive RGB orthomosaic and DSM processed from the Bird Shoal sorties is presented in Figure 2, along with GCP and checkpoint locations. A summary of flights as well as basic mosaic and DSM quality can be seen in Table 1. Actual GSD was very similar to planned GSD despite high wind gusts during the missions (Table 1). Flight 1 was ended prematurely when strong winds disrupted the UAS's planned flight path. Thus, the DSM from this mission did not extend as far east as the others and had a sparser point cloud density. The dataset resulting from the combined processing of all three RTK flights had the largest footprint (~0.21 km^2), the densest point cloud (361 pts/m^3), and a GSD of 2.28 cm.

Table 2. *Accuracy assessment of UAS DSMs with and without GCP correction compared to a GNSS checkpoint survey. Seven checkpoints were used for horizontal error assessment, and 53 checkpoints were used for vertical error assessment. When used, six GCPs were used for correction.*

		RMS Error (m)		Sigma (m)		Offset (m)	
Flight Number	UAS GPS	*X/Y*	Vertical	*X/Y*	Vertical	*X/Y*	Vertical
GCP-Corrected							
1	Survey	0.020/0.027	0.073	0.019/0.026	0.072	0.015/0.019	0.043
2	Survey	0.017/0.030	0.031	0.017/0.030	0.030	0.015/0.025	0.024
3	Survey	0.029/0.027	0.036	0.027/0.025	0.036	0.019/0.023	0.029
4	Mapping	0.039/0.032	0.089	0.038/0.027	0.070	0.031/0.021	0.068
1-3	Survey	0.016/0.022	0.027	0.013/0.019	0.028	0.013/0.018	0.022
Not GCP-Corrected							
1	Survey	0.025/0.132	0.092	0.156/0.032	0.078	0.020/0.128	0.063
2	Survey	0.027/0.067	0.080	0.026/0.048	0.045	0.019/0.058	0.068
3	Survey	0.064/0.106	0.123	0.051/0.044	0.056	0.060/0.096	0.111
4	Mapping	0.709/1.162	1.157	0.413/0.159	0.684	0.583/1.152	1.039
1–3	Survey	0.037/0.049	0.064	0.019/0.016	0.041	0.031/0.047	0.052

Field Survey Time

The four UAS sorties over the study area required a total of 3.5 hours. This included a combined 68 minutes of flight time (Table 1) as well as an hour of mission planning comprising weather assessments and building flight plans. There was also a 10-minute preflight check for each flight comprising an equipment/aircraft assessment and a battery swap, as well as 1 hour devoted to deploying GCPs and surveying checkpoints. The ground crew comprised a remote pilot acting in a supervisory role and two technicians acting as an observer and a survey GPS operator. The eBee was $16,490 (June 2016 price), and the eBee RTK was $31,900 (June 2016 price). (At the time of writing, respective prices for the eBee and eBee RTK had dropped to $14,990 and $26,990.) The Pix4D software used to generate DSMs was $4990 (June 2016 price, annual subscription).

The TLS of two 2500-m^2 study plots required approximately 4.5 hours. Setup, including placement and surveying of TLS reflectors, required ~0.75 hours at each plot. Both locations were scanned from four positions, which required ~1.3 hours total at each plot, with an additional half hour for equipment teardown at the end of the field day. The crew comprised a TLS operator acting in a supervisory role, with two technicians assisting with reflector deployment and scanner repositioning. The total cost of the TLS equipment was $75,000. Both the TLS crew and the UAS crew used a $20,000 survey GNSS unit to record GCP positions and to register the location of the TLS equipment. Personnel costs for UAS and TLS crews were similar—approximately $95/h.

Table 3. *Accuracy assessment of UAS point clouds with and without GCP correction compared to a GNSS checkpoint survey. Seven checkpoints were used for horizontal error assessment, and 53 checkpoints were used for vertical error assessment. When used, six GCPs were used for correction.*

Flight Number	UAS GPS	RMS Error (m) Vertical	Sigma (m) Vertical	Offset (m) Vertical
GCP-Corrected				
1	Survey	0.080	0.079	0.046
2	Survey	0.035	0.035	0.027
3	Survey	0.036	0.035	0.030
4	Mapping	0.075	0.062	0.057
1–3	Survey	0.025	0.025	0.021
Not GCP-Corrected				
1	Survey	0.082	0.080	0.051
2	Survey	0.069	0.040	0.059
3	Survey	0.119	0.058	0.105
4	Mapping	1.005	0.567	0.907
1–3	Survey	0.051	0.037	0.041

UAS and GNSS Comparisons

Accuracy assessments of UAS-derived DSMs and point clouds referenced to GNSS checkpoints can be seen in Tables 2 and 3, respectively. The DSMs and point clouds from RTK-equipped UAS were very similar to one another, with accuracy statistics differing by a maximum of 0.015 m. Because the point cloud is an intermediate product for many data end users and interpolated surfaces are required for change analysis (Mancini *et al.*, 2013), the accuracy investigation here focuses on DSMs.

When processing images from individual RTK-equipped flights without GCP correction, DSM elevation averaged 0.063–0.111 m from GNSS survey heights, corresponding to a vertical RMS error between 0.080 and 0.123 m (Table 2). The greatest vertical error consistently accrued around the easternmost sections of the study area (Figure 3). When error was parsed by habitat type, the DSM elevation on the foreshore (Figure 2C) was least accurate, averaging 0.089 m from GNSS elevations ($\sigma = 0.057$ m). The DSM elevations on the vegetated dune field were more accurate, averaging 0.080 m from GNSS elevations ($\sigma = 0.040$ m), and elevations were most accurate on the washover terrace, averaging 0.072 m from GNSS elevations ($\sigma = 0.049$ m). Horizontal error varied but was under or around 10 cm. In addition to being offset from the GNSS points, DSM elevations from separate RTK flights were also offset from one another, with the elevation range between flights averaging 0.166 m. The DSM derived from UAS with a standard GPS system was substantially less accurate than those from RTK flights, with around 1 m of vertical and horizontal error. Conversely, the DSM produced by combining all RTK flight imagery compared better to GNSS elevation than DSMs from any single flight.

When processing the same DSMs with GCP correction, accuracy improved in all categories, and error distributions were compressed (Figure 4). The DSM elevation from individual RTK flights averaged 0.024–0.043 m from GNSS points, corresponding to an RMS error of 0.031–0.073 m (Table 2), and horizontal RMS error was reduced to 0.030 m or less. When

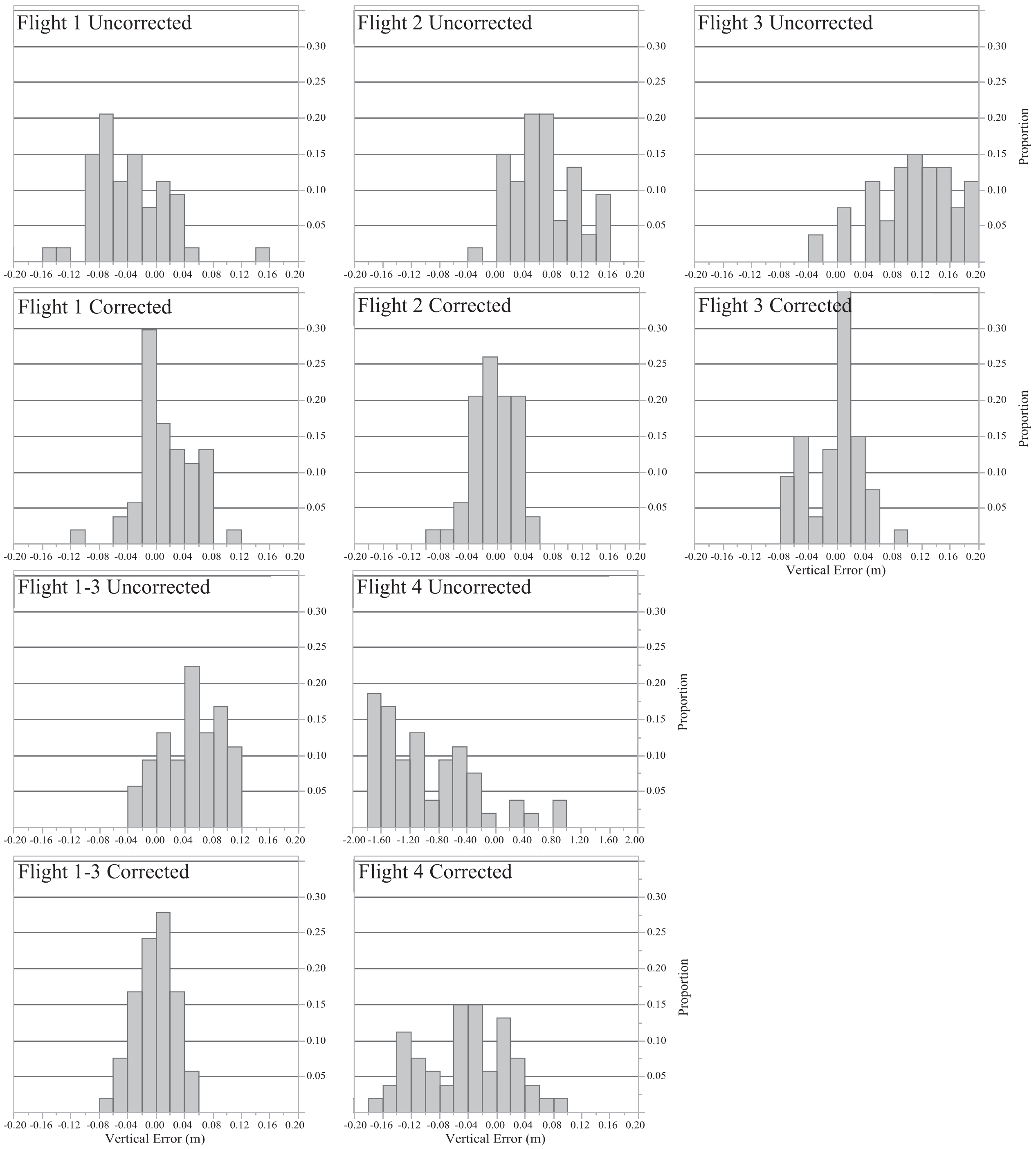

Figure 3. Spatial distribution for the vertical errors of (A) non-GCP-corrected RTK flights and (B) GCP-corrected RTK flights. Flights 1, 2, and 3 are depicted by different-sized points layered on top of one another, and warmer colors indicate greater error for that point relative to the GNSS checkpoints.

compared with one another, the DSM elevations from separate RTK flights were similar, offset by an average of 0.051 m. The GCP correction mitigated some spatial error trends; relatively less error was concentrated around the eastern boundary and scarp regions, with relatively more error across the center of the washover terrace (Figure 3). When parsed by habitat type, the DSM elevation on the foreshore (Figure 2C) was once again the least accurate, averaging 0.035 m from GNSS elevations (σ = 0.027 m). Elevations on the washover terrace were closer to GNSS elevations, averaging 0.029 m from GNSS elevations (σ =

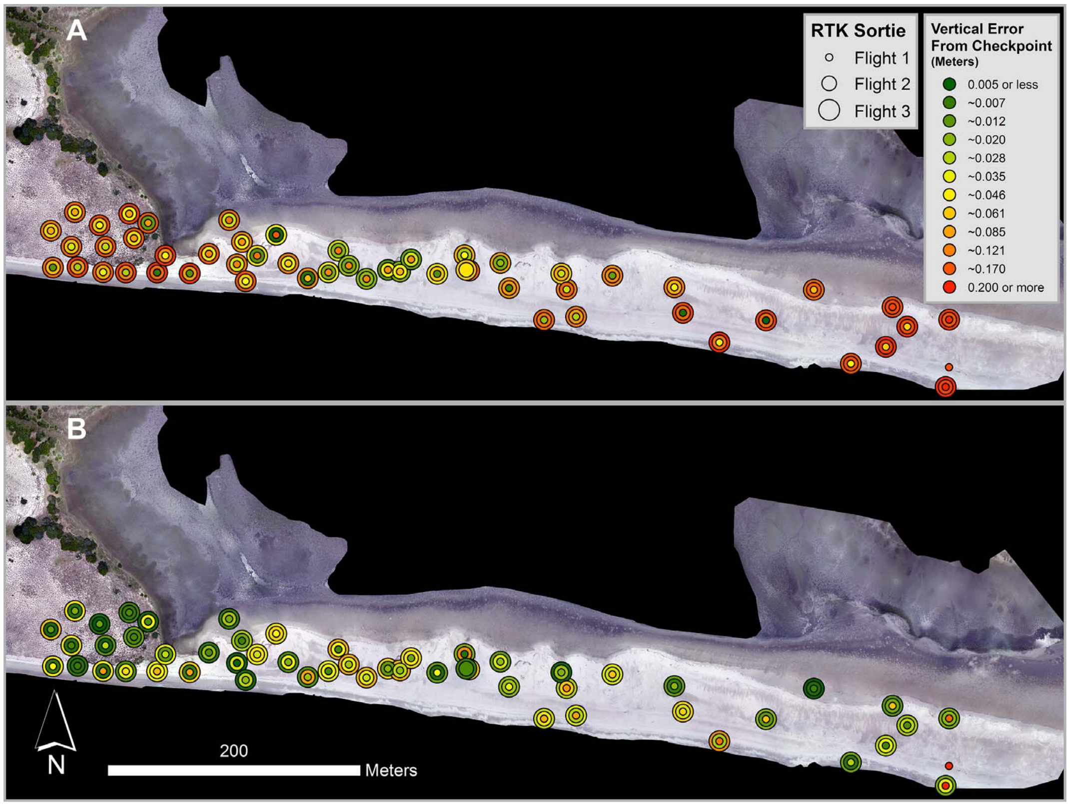

Figure 4. Distribution of the vertical error from each checkpoint to the surface of UAS DSMs. Frequency is measured in proportion of total checkpoints. Note the change in the *x*-axis scale between corrected and uncorrected Flight 4 histograms, attributable to the very large difference in error between these datasets. (Color for this figure is available in the online version of this article.)

0.020 m), and DSM elevations were most accurate on the vegetated dune field, averaging 0.015 m from GNSS elevations ($\sigma = 0.017$ m). The GCP correction improved the accuracy of the DSM derived from standard GPS-equipped UAS by more than an order of magnitude, with heights averaging 0.060 m from GNSS elevation. The accuracy of the combined-flight DSM also improved but was not substantially different than the accuracy of DSMs derived from individual RTK flights.

TLS and UAS DSM Comparison

The DSMs from TLS and GCP-corrected UAS-derived point clouds were very similar in the washover terrace plot, with a 0.042 m average elevation difference between surfaces (σ = 0.035). Minor surface divergence occurred on the sides of some dunes and in isolated areas of sandy beach (Figure 5D). The TLS surfaces were significantly farther away from the GNSS checkpoints (Wilcoxon Rank Sum test, $S = 46$, $P = 0.024$) because of occlusion effects around low dunes. The TLS and UAS DSMs were less similar in the vegetated dune plot, with an average difference of 0.082 m between surfaces ($\sigma = 0.072$). North of the erosional escarpment, divergences were frequent and associated with the areas around vegetation patches, but surfaces conflicted less on the foreshore where there was no vegetation (Figure 5C). The TLS surface was again significantly farther from the GNSS checkpoints than the UAS surface (Wilcoxon Rank Sum test, $S = 105$, $P = 0.010$), and offset was greater in this area (Figure 6). Individual DSMs derived from TLS and UAS within the TLS regions can be seen in Figure 7. The TLS consistently generated artifacts around vegetation and low dunes, taking the form of coarse, lengthened relief on the illuminated face of objects and smooth aggregations of additional volume on the shadowed face. Instead, the SfM image processing generated artifacts on regions of flat, sandy, and unvegetated beach, particularly on the foreshore (Figure 7B,D). These artifacts were typically more disbursed and of smaller amplitude than TLS artifacts. Considered across the entire 0.2-km^2 UAS study region, scattered artifacts were typically 1–30 cm high but occasionally formed groups of 0.5–1.0 m diameter ditches or spikes up to 1 m in depth (Appendix B).

DISCUSSION

This study highlights the strengths of fixed-wing UAS in collecting coastal elevation datasets and provides guidance for appropriate flight planning and GPS equipment selection in the sandy beach environment. For UAS sorties that supply data to coastal managers, the selected airframe, sensor, flight plan, and GPS are strongly influenced by the spatial scale and accuracy relevant to policymaking.

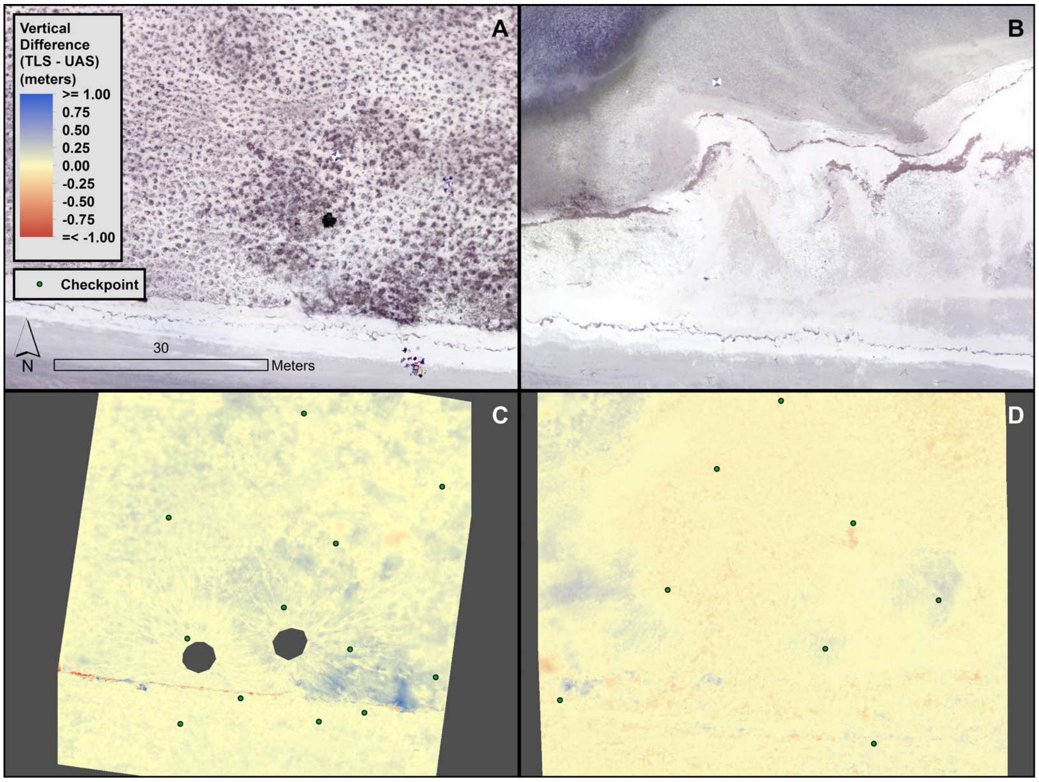

Figure 5. Elevation difference between a TLS-derived DSM and UAS-derived DSM with RGB mosaics shown for reference. Blue represents sections where the TLS surface was above the UAS surface, and red represents sections where the UAS surface was above the TLS surface. Two areas are shown: the vegetated dune plot (A) and (C) and a washover terrace plot (B) and (D). (Color for this figure is available in the online version of this article.)

The absolute spatial accuracy of a DSM or orthomosaic hinges on multiple factors, including the amount of available light, sensor settings, prevailing wind conditions, the structure of the flight plan, the texture of the surface being imaged, and the GPS unit installed on the UAS. For instance, factors such as image format, image overlap, and flight altitude can influence the number of keypoints generated and matched by increasing resolution and by including features on the ground in more images. In this study, equipping an RTK GPS on the UAS decreased the level of vertical error from meters to around 10 cm or less. However, the ebee RTK UAS did not achieve its marketed precision (<5 cm vertical error) without the use of GCPs, despite nominal (0.03–0.05 m) error estimations by the GPS unit during flight (but see Table 1, Flight 3 Notes). This is largely attributable to the solar position during the time of the surveys, as well as the inherent texture and color variation on the surfaces being imaged.

Sandy beaches can be challenging environments for SfM photogrammetry. When dunes, vegetation, wrack, or shells are absent, bodies of sand in RGB images have low color variability, leaving relatively few unique pixels (keypoints) for SfM to match between images. A high sun angle can greatly compound these challenges, overexposing sections of sand or eliminating shadows cast by low-level elevation variability on the sandy surface. This weakens color/reflectance gradients, undermining keypoint generation. In this study, the maximum daily sun elevation occurred during Flight 1 and remained within 10° of the maximum for the remaining flights. This contributed to uncorrected flights' eastward vertical error distribution (Figure 3A) because wide stretches of imagery with low keypoint availability tend to propagate error as they mosaic together. The DSM produced from the combined imagery of all three RTK flights had the best vertical accuracy of any single uncorrected DSM (Table 2); the greater number of overlapping images provided the SfM process more keypoint matching opportunities. GCP correction of the individual RTK DSMs with six control points brought vertical error below 5 cm (Table 2) and eliminated spatial error propagation across the dataset (Figure 3B), mitigating the accuracy challenges in this coastal environment.

The UAS and TLS-derived DSMs had high conformance on the washover terrace but diverged significantly in vegetated regions and, to a lesser extent, on the foreshore. The surface elevation differences are explained by the different ways these methods generate artifacts. TLS often struggles when scanning complex terrain (Eltner and Baumgart, 2015; Eltner, Mulsow, and Maas, 2013; Feagin *et al.*, 2014); elevated objects occlude laser beams, creating scan shadows that are then filled in during interpolation. In this study, occluded regions encompassed the areas that were most different between UAS and TLS surfaces. Occlusion effects were pronounced on areas with vegetation, resulting in deviations in some areas up to 1 m in

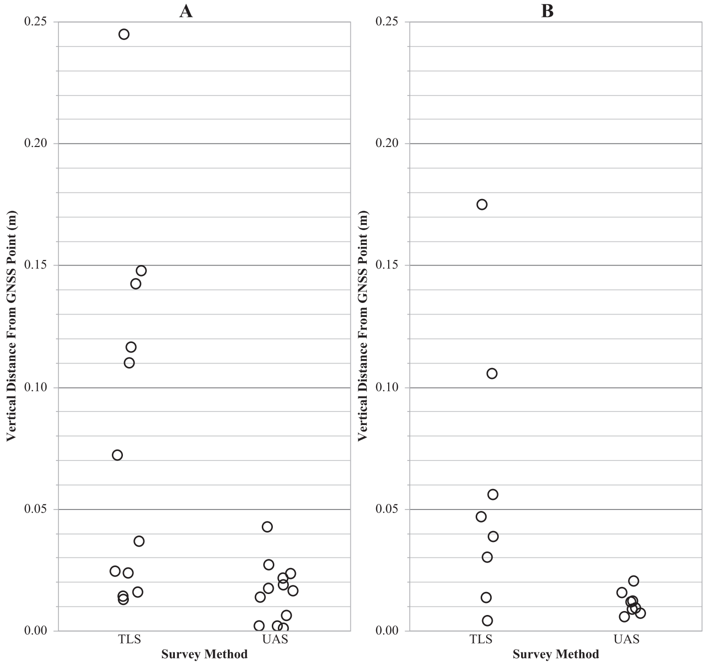

Figure 6. The absolute vertical distance of TLS and UAS surfaces from GNSS points at (A) the vegetated dune plot and (B) the washover terrace plot.

height (Figure 7A). Occlusion artifacts formed around low dunes as little as 30 cm in height, despite a DSM mosaiced from four scans at four different perspectives (Figure 7C). The TLS point-cloud density also decreases with distance from the laser scanner, which likely contributed to the observed errors. Conversely, TLS performed very well on the flat areas of the beach, outputting smooth surfaces with minimal artifacts (Figure 7C).

UAS and SfM processing were not confounded by elevated objects, outputting accurate, artifact-free representations of dune mounds and vegetated berms. SfM instead generated DSM artifacts on areas of UAS imagery with especially homogenous texture, such as flat planes of featureless sand devoid of beach wrack or shells. These areas lacked strong color/reflectance gradients, removing the basis for keypoint generation and stereoscopic comparison. The sun's position at the time of the survey is an important factor for artifact generation and DSM accuracy, and the most pronounced artifacts and least accurate surfaces were found on the foreshore (Figure 2), which faced most perpendicular to the sun. These areas were also exposed to wave run-up, which pushed away features such as shells and wrack and flattened small-scale mounds of sand that could have otherwise provided texture and shadow. Artifacts were localized to sparse or empty regions of the point cloud and were unaffected by GCP correction. The washover terrace (Figure 2C) was of relatively high accuracy and had fewer artifacts because it was not smoothed or cleared of beach wrack by regular wave run-up, and low lying dunes created texture and shadow, providing keypoints even in less-than-optimal light conditions. The vegetated dune field (Figure 2C) was artifact-free and very accurate in GCP-corrected DSMs because clumps of low vegetation were good surfaces for keypoint generation. Accuracy of uncorrected DSMs fared worse in this area because around high relief, an object's (such as vegetation clumps or a scarp line) horizontal error compounds vertical error because of the DSM's additional offset. No checkpoints deployed on the tidal flat (Figure 2C) to directly assess accuracy occurred, but this section of the DSM was artifact-free because of good image texture. Despite being topographically flat and comprising fine-grained silt and mud, this area had a high coverage of small mounds, holes, and other signs of bioturbation that contrasted well in imagery. While accuracy did differ between habitat types, the average difference was never above 0.02 m. Conversely, a strong difference in artifact presence occurred between some habitat classes, particularly on the foreshore. The DSM produced by combining imagery from separate flights had the least artifact extent and severity (Appendix B). The Sony DSC-WX220 sensor selected shutter speeds automatically but also inconsistently, and some images were collected at shutter speeds as long as 1/300 seconds. This likely increased the severity and extent of artifacts by introducing motion blur into images, further homogenizing image texture.

In spite of processing challenges on some sandy, planar areas of beach, there is a strong argument for using UAS to collect municipal-scale datasets for coastal managers. The 4.5 hours of TSL in this study resulted in two DSMs amounting to 0.005 km^2 area combined. Using a mobile TLS (a vehicle-mounted TLS with integrated GNSS and inertial measurement unit) would have increased the area of the DSM but also would have adversely impacted the ecosystem by trampling flora, fauna, and dunes. Despite operating during unfavorable wind condi-

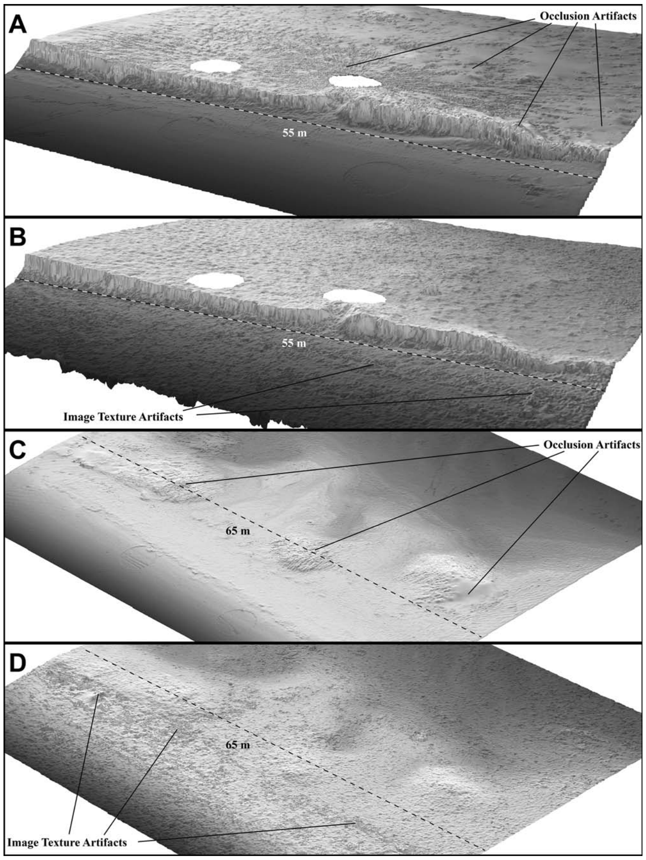

Figure 7. (A) TLS and (B) UAS DSM within the TLS scanning boundaries in the vegetated dune plot and (C) TLS and (D) UAS DSM within the washover terrace.

tions, the 3.5 hours of UAS surveys resulted in four flights, each producing a DSM more than an order of magnitude larger than the total combined TLS area. This confirms that UAS can collect datasets at municipal scales that are largely impractical with TLS and with comparable elevation accuracy if GCPs are used. While GCP deployment remains a consistent way of reducing error, municipal scale data products such as vulnerability assessments and storm surge models typically do not require <5 cm vertical error and are also insensitive to our observed difference in accuracy between habitat classes. Thus, studies using survey-GPS-equipped UAS can collect certain types of management-relevant coastal datasets without using GCPs. To avoid error propagation over large-scale sandy beaches, care must be taken to plan flights during solar angles that create contrast on the beach. This factor may be particularly important when surveying beaches with a wide foreshore and narrow or nonexistent dune field. DSMs produced by UAS equipped with mapping-grade GPS systems are management-relevant only with GCP correction because of their large (>1 m) native vertical error. However, mapping-grade systems may be sufficient for color or multispectral mosaics intended for habitat mapping because this product does not have a vertical component, and ~2 m of horizontal error may be negligible for many management-scale landscape classifications. It should be noted that regardless of the hardware used on the UAS, integrating GCPs into a survey can act as an accuracy safety net in the case of GNSS malfunctions or loss of RTK fix, as occurred during Flight #3 (Table 1). Ultimately, UAS equipment should be selected based on the accuracy needed by managers and policymakers for a specific project, and these requirements should be explicitly determined well before any flights occur.

When fine-scale change detection is required, it is recommended that surveys fully leverage GCPs, as the ~17 cm elevation range found across the uncorrected RTK datasets is problematic for this application. For these surveys, as well as data intended for erosion or sediment transport modeling, addressing artifact-driven elevation error also becomes essential because artifact clusters may create false beach rugosity. The artifacts discussed in this study can be avoided through appropriate flight planning or eliminated in postprocessing. Increasing image overlap, using an appropriately high shutter speed (*i.e.* 1/2000 seconds), choosing a small GSD, or processing images from multiple flights together can reduce artifact generation, but flying sorties during low sun elevation is likely most critical. During a separate survey, keypoint matching in the Bird Shoal study area could be increased 5–10 times and artifacts almost entirely eliminated by planning flights during solar elevations of ~17° with a GSD of 2.5 cm (Appendix B and C). Timing flights around storms may also be necessary for artifact reduction. Significant storm-driven overwash could smooth, bury, or disturb sections of the beach, such as the washover terrace and tidal flat, which would otherwise have adequate image texture. Thus, it may be beneficial to delay poststorm surveys for several days or weeks until small scale rugosity, wrack, shells, and signs of bioturbation are again visible on the beach. Future studies can test images in the nonvisible spectrum similar to Bühler *et al*. (2017), who used infrared images to improve the texture available on fresh alpine snow packs. Because the artifacts in this study are highly localized to specific low spectral variance surfaces, there is also potential to automatically detect and eliminate them in postprocessing with computer vision algorithms.

CONCLUSIONS

This study provides coastal managers with guidelines on how to select appropriate UAS equipment for coastal morphology surveys and provides accuracy comparisons for two classes of GPS-equipped fixed-wing UAS, which are airframes appropriate for municipal-scale sorties. The role of GCPs is placed into management context with mapping-grade UAS and newer survey-grade UAS, as these systems have different degrees of reliance on control points. The influence of habitat coverage and beach morphology on sfM processing is discussed, with implications for flight planning around solar elevation and storm events. These considerations will help managers match appropriate equipment and flight plans to monitoring objectives and accuracy requirements. Notably, the eBee and eBee RTK used in this study are now dated. Fixed-wing platforms currently exist with two times the aerial endurance and lift increasingly more advanced sensor packages that include multispectral and LIDAR modules. Providing civil regulations does not limit their application; in the coming years, UAS will be practical for surveying increasingly larger municipalities while providing accuracy equal to or better than fine-scale TLS. The TLS systems are also advancing; however, increases in target range, accuracy, and measurement rate will not overcome challenges associated with working in fragile, low-relief coastal environments and occlusion effects associated with vegetation and dunes. When combined appropriately with the guidelines in this study, UAS can offer coastal managers a frequent and affordable means of assessing coastal resilience in the face of sea-level rise and dramatic storm events at a local scale often overlooked.

LITERATURE CITED

Barneveld, R.J.; Seeger, M., and Maalen-Johansen, I., 2013. Assessment of terrestrial laser scanning technology for obtaining high-resolution DEMs of soils. *Earth Surface Processes and Landforms*, 38(1), 90–94. doi:10.1002/esp.3344

Bühler, Y.; Adams, M.S.; Stoffel, A., and Boesch, R., 2017. Photogrammetric reconstruction of homogenous snow surfaces in alpine terrain applying near-infrared UAS imagery surfaces in alpine terrain. *International Journal of Remote Sensing*, 38(8–10), 2029–2036. doi:10.1080/01431161.2016.1275060

Casella, E.; Rovere, A.; Pedroncini, A.; Mucerino, L.; Casella, M.; Cusati, L.A.; Vacchi, M., and Firpo, M., 2014. Estuarine, coastal and shelf science study of wave runup using numerical models and low-altitude aerial photogrammetry: A tool for coastal management. *Estuarine, Coastal and Shelf Science*, 149, 160–167. doi:10.1016/j.ecss.2014.08.012

Delacourt, A.C.; Allemand, P.; Jaud, M.; Grandjean, P.; Deschamps, A.; Ammann, J., and Suanez, S., 2009. An unmanned helicopter for imaging coastal areas. *In:* Roberts, T.M.; Rosati, J.D., and Wang, P. (eds.), *Proceedings of the 10th International Coastal Symposium*, *Journal of Coastal Research*, Special Issue No. 59, pp. 1489–1493.

Eltner, A. and Baumgart, P., 2015. Accuracy constraints of terrestrial Lidar data for soil erosion measurement: Application to a Mediterranean field plot. *Geomorphology*, 245, 243–254. doi:10.1016/j.geomorph.2015.06.008

Eltner, A.; Mulsow, C., and Maas, H., 2013. Quantitative measurement of soil erosion from TLS and UAV data. *International Archives of the Photogrammetry, Remote Sensing, and Spatial Information Sciences*, XL-1(W2), 4–6.

Feagin, R.A.; Williams, A.M.; Popescu, S.; Stukey, J., and Washington-Allen, R.A., 2014. The use of terrestrial laser scanning (TLS) in dune ecosystems: The lessons learned. *Journal of Coastal Research*, 30(1), 111–119.

Golden Software. 2012. *Surfer 11*. Golden, Colorado: Golden Software.

Gómez-Gutiérrez, Á.; de Sanjosé-Blasco, J.; Lozano-Parra, J.; Berenguer-Sempere, F., and de Matías-Bejarano, J., 2015. Does HDR pre-processing improve the accuracy of 3-D models obtained by means of two conventional SfM-MVS software packages? The case of the Corral del Veleta rock glacier. *Remote Sensing*, 7(8), 10269–10294. doi:10.3390/rs70810269

Gonçalves, J.A. and Henriques, R., 2015. UAV photogrammetry for topographic monitoring of coastal areas. *ISPRS Journal of Photogrammetry and Remote Sensing*, 104, 101–111. doi:10.1016/j.isprsjprs.2015.02.009

Gross, J.W. and Heumann, B.W., 2016. A statistical examination of image stitching software packages for use with unmanned aerial systems. *Photogrammetric Engineering & Remote Sensing*, 82(6), 419–425. doi:10.14358/PERS.82.6.419

Hart, D.E. and Knight, G.A., 2009. Geographic information system assessment of tsunami vulnerability on a dune coast. *Journal of Coastal Research*, 25(1), 131–141. doi:10.2112/07-0960.1

Harwin, S. and Lucieer, A., 2012. Assessing the accuracy of georeferenced point clouds produced via multi-view stereopsis from unmanned aerial vehicle (UAV) imagery. *Remote Sensing*, 4(6), 1573–1599. doi:10.3390/rs4061573

Karsky, D., 2004. *Comparing Four Methods of Correcting GPS Data: DGPS, WAAS, L-Band, and Postprocessing*. Missoula, Montana: U.S. Department of Agriculture, Forest Service, Missoula Technology and Development Center, 6p.

Klemas, V.V., 2009. The role of remote sensing in predicting and determining coastal storm impacts. *Journal of Coastal Research*, 25(6), 1264–1275.

Klemas, V.V., 2015. Coastal and environmental remote sensing from unmanned aerial vehicles: An overview. *Journal of Coastal Research*, 31(5), 1260–1267.

LaMarca, A. and Lara, E.D., 2008. The global positioning system. *In:* LaMarca, A.; Lara, E.D., and Satyanarayanan, M. (eds.), *Location Systems: An Introduction to the Technology Behind Location Awareness*. Williston, Vermont: Morgan & Claypool, pp. 6–18.

Mancini, F.; Dubbini, M.; Gattelli, M.; Stecchi, F.; Fabbri, S., and Gabbianelli, G., 2013. Using unmanned aerial vehicles (UAV) for high-resolution reconstruction of topography: The structure from motion approach on coastal environments. *Remote Sensing*, 5(12), 6880–6898. doi:10.3390/rs5126880

Merrick. 2017. *Mars 7*. Greenwood Village, Colorado: Merrick.

Papakonstantinou, A.; Topouzelis, K., and Pavlogeorgatos, G., 2016. Coastline zones identification and 3D coastal mapping using UAV spatial data. *International Journal of Geo-Information*, 5(75), 1–14. doi:10.3390/ijgi5060075

Pilkey, O.H.; Cooper, J.A.G., and Lewis, D.A., 2009. Global distribution and geomorphology of fetch-limited barrier islands. *Journal of Coastal Research*, 25(4), 819–929.

RIEGL LMS. 2013. *RiSCAN Pro*. Horn, Australia: RIEGL Laser Measurement Systems.

Sasse, D.B., 2003. Job-related mortality of wildlife workers in the United States, 1937–2000. *Wildlife Society Bulletin*, 31(4), 1000–1003.

Schneider, A.; Gerke, H.H.; Maurer, T.; Seifert, S.; Nenov, R., and Hüttl, R.F., 2012. Evaluation of remotely-sensed DEMs and modification based on plausibility rules and initial sediment budgets of an artificially-created catchment. *Earth Surface Processes and Landforms*, 37(7), 708–725. doi:10.1002/esp.2274

Schürch, P.; Densmore, A.L.; Rosser, N.J.; Lim, M., and McArdell, B.W., 2011. Detection of surface change in complex topography using terrestrial laser scanning: Application to the Illgraben debris-flow channel. *Earth Surface Processes and Landforms*, 36(14), 1847–1859. doi:10.1002/esp.2206

SenseFly. 2013. *eMotion2*. Lausanne, Switzerland: SenseFly.

SenseFly. 2013. *Pix4D Mapper*. Lausanne, Switzerland: SenseFly.

Wing, M.G.; Eklund, A., and Kellogg, L.D., 2005. Consumer-grade global positioning system (GPS) accuracy and reliability. *Journal of Forestry,* 103(4), 169–173.

APPENDIX A GPS System Specifications

Ebee Standard GPS System	Model LEA-5H
Receiver type	50 channels
Signals tracked	GPS: L1, C/A Code GALILEO: L1
Acquisition time	Cold start: 29 seconds Warm start: 29 seconds Hot start: <1 second Reacquisition: <1 second
Accuracy	*H*: <2.5 m; *V*: <3 m
Ebee RTK GPS System	
Receiver type	226 channels
Signals tracked	GPS: L1, L2 GLONASS: L1, L2
Acquisition time	Cold start: <60 seconds Warm start: <35 seconds Hot start: <10 seconds Reacquisition: <1 second
Onboard RTK correction	20 Hz
Upstream correction:	1 Hz
RTK Transmission protocol:	RTCM-3.x, RTCM-2.x
Accuracy:	Standalone: *H*: 1.2 m; *V*: 1.8 m RTK: *H*: 0.015 m; *V*: 0.020 m (relative to base station)

APPENDIX B
UAS Study Area Artifact Comparison

The following series of figures depicts different DSM sections in the overall UAS study region. Each figure shows (A) an RGB reference mosaic, (B) a DSM section from RTK Flight 2, (C) a DSM section from the project combining images from RTK Flights 1–3, and (D) DSM from an RTK flight done in November of 2016. The November flight occurred during a solar elevation of ∼17° and was executed with an ebee RTK, a similar GSR, and similar sensor package as the sorties in June. The flights in June occurred during a solar elevation of 70–77°.

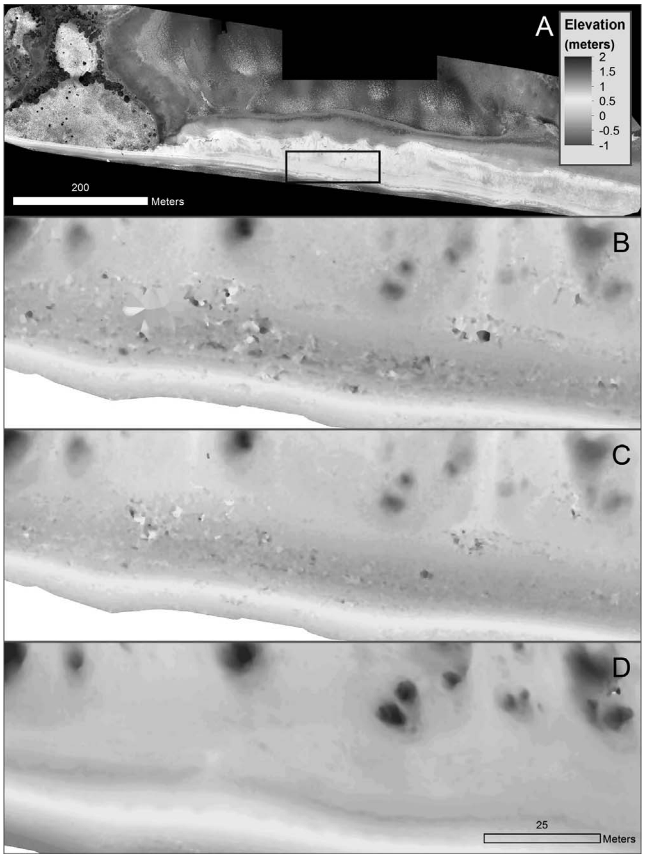

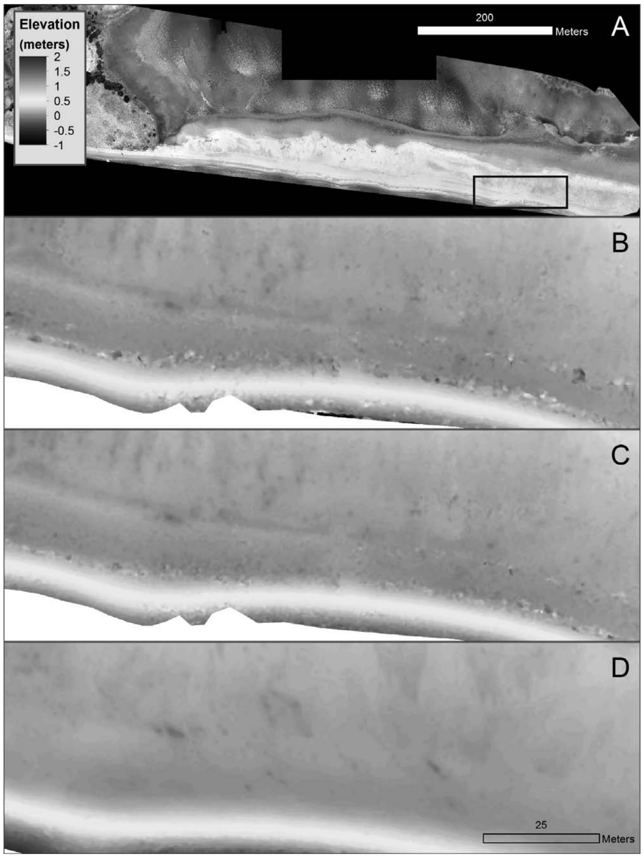

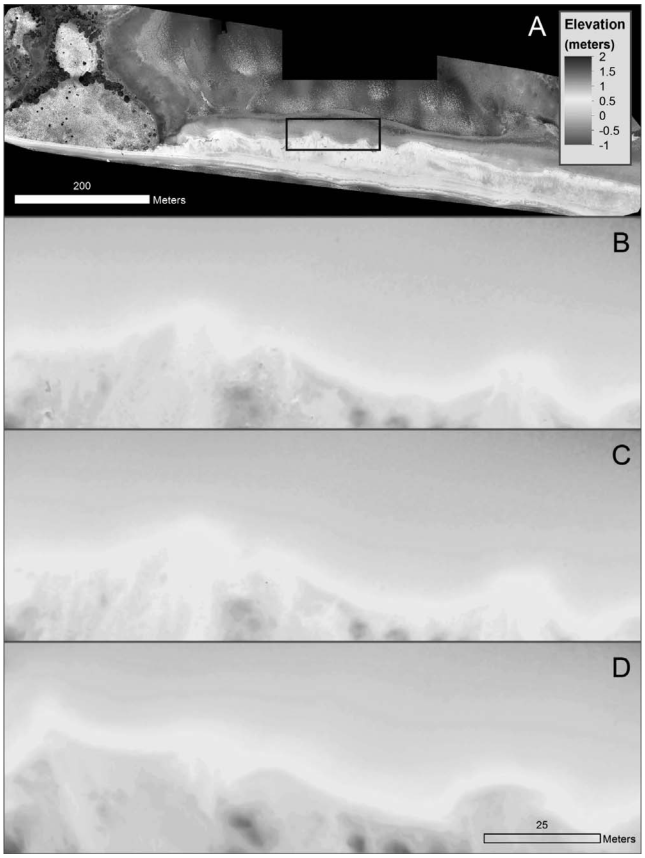

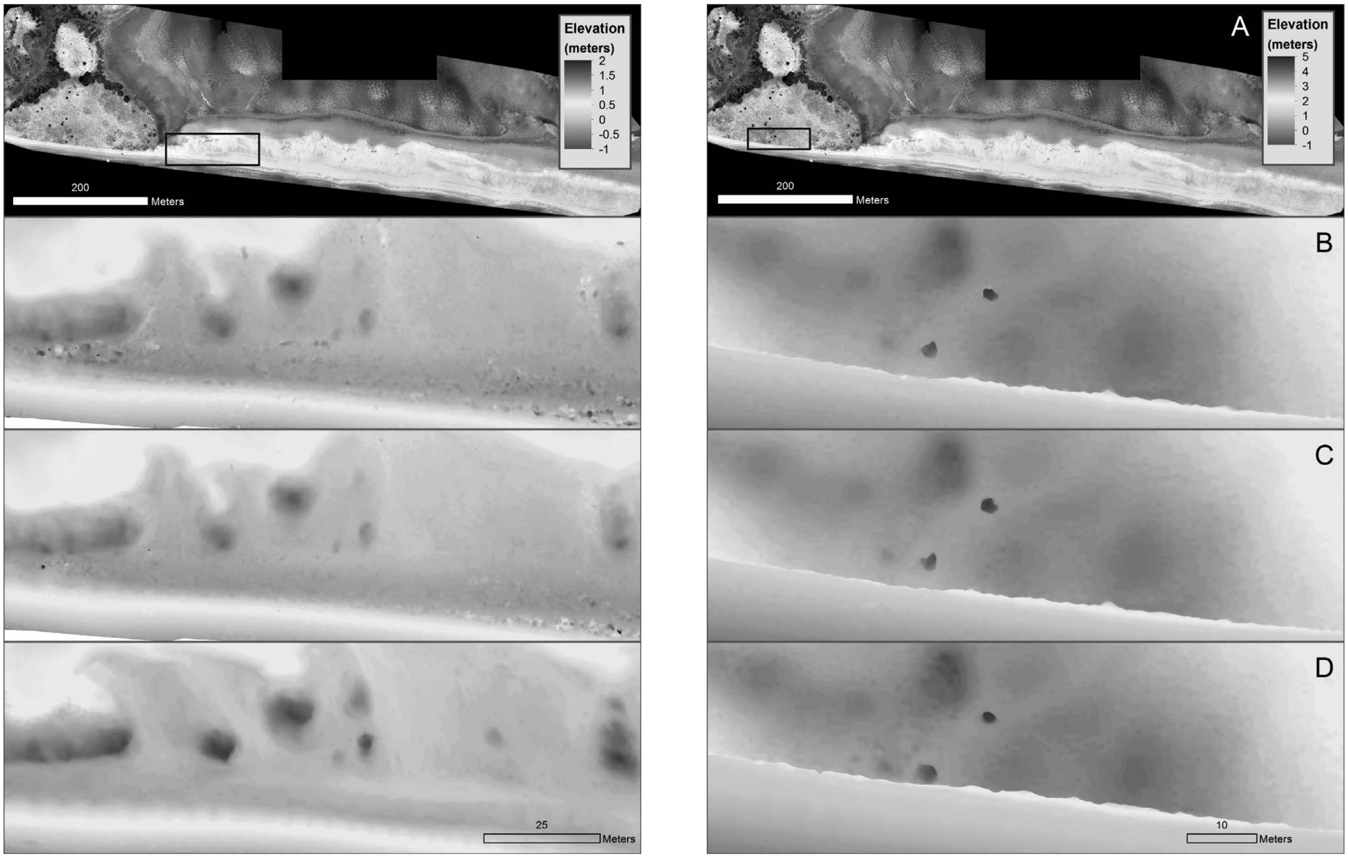
Elevation
(meters)
2
1.5
1
0.5
0
-0.5
-1
200
Meters
25
Meters
A
Elevation
(meters)
5
4
3
2
1
0
-1
200
Meters
B
C
D
10
Meters

APPENDIX C

Keypoint Matching Comparision

The following figures were drawn from the Pix4D Mapper quality reports for (A) the project that combined all June RTK imagery and (B) the project from the November 2016 flight. Note the difference in the number of keypoints matched within the original UAS study area between June and November.

A

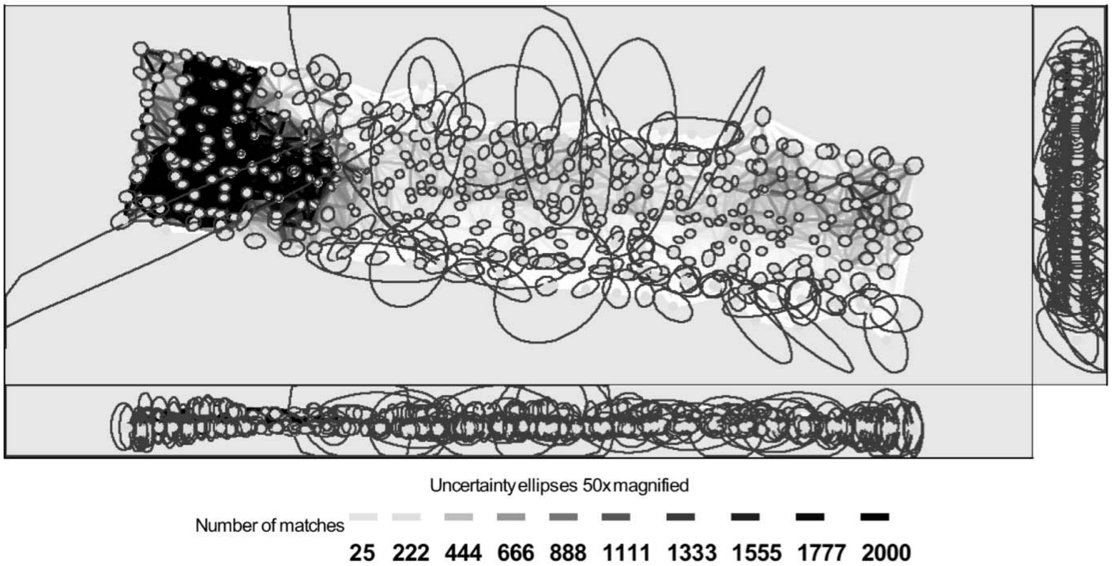

B